

Creative Commons Attribution 4.0 International (CC BY 4.0)

<https://creativecommons.org/licenses/by/4.0/>

Access to this work was provided by the University of Maryland, Baltimore County (UMBC) ScholarWorks@UMBC digital repository on the Maryland Shared Open Access (MD-SOAR) platform.

**Please provide feedback**

Please support the ScholarWorks@UMBC repository by emailing [scholarworks-group@umbc.edu](mailto:scholarworks-group@umbc.edu) and telling us what having access to this work means to you and why it's important to you. Thank you.

# A COMPUTER-AIDED SYSTEM FOR MASS DETECTION AND CLASSIFICATION IN DIGITIZED MAMMOGRAMS

SHENG-CHIH YANG<sup>1,2</sup>, CHUIN-MU WANG<sup>2</sup>, YI-NUNG CHUNG<sup>3</sup>, GIU-CHENG HSU<sup>4</sup>, SAN-KAN LEE<sup>5</sup>,  
PAU-CHOO CHUNG<sup>1</sup>, CHEIN-I CHANG<sup>6</sup>

<sup>1</sup>Department of Electrical Engineering, National Cheng Kung University, Tainan, Taiwan

<sup>2</sup>Department of Computer Science and Information Engineering, National Chin Yi Institute of Technology, Taichung, Taiwan

<sup>3</sup>Department of Electrical Engineering, Da-Yeh University, Chunghua, Taiwan

<sup>4</sup>Department of Radiology, Tri-Service General Hospital and National Defense Medical Center, Taipei, Taiwan

<sup>5</sup>Administrative Office, Suao Veterans Hospital, Yilan, Taiwan

<sup>6</sup>Remote Sensing Signal and Image Processing Laboratory, Department of Computer Science and Electrical Engineering, University of Maryland, Baltimore, MD, USA

## ABSTRACT

*This paper presents a computer-assisted diagnostic system for mass detection and classification, which performs mass detection on regions of interest followed by the benign-malignant classification on detected masses. In order for mass detection to be effective, a sequence of preprocessing steps are designed to enhance the intensity of a region of interest, remove the noise effects and locate suspicious masses using five texture features generated from the spatial gray level difference matrix (SGLDM) and fractal dimension. Finally, a probabilistic neural network (PNN) coupled with entropic thresholding techniques is developed for mass extraction. Since the shapes of masses are crucial in classification between benignancy and malignancy, four shape features are further generated and joined with the five features previously used in mass detection to be implemented in another PNN for mass classification. To evaluate our designed system a data set collected in the Taichung Veteran General Hospital, Taiwan, R.O.C. was used for performance evaluation. The results are encouraging and have shown promise of our system.*

Biomed Eng Appl Basis Comm, 2005(October); 17: 215-228.

Keywords: Classification. Detection. Entropic thresholding. Fractal dimension (FD). Joint entropy (JE). Local entropy (LE). Probabilistic neural network (PNN). Spatial gray level difference matrix (SGLDM). Texture feature. Shape feature.

## 1. INTRODUCTION

Mammography is by far the only effective screening method for detection of breast cancer in early stage [1]. Although mammography is considered high effective, presently the diagnosis is conducted based on physicians' personal experiences, which

Received: Nov 6, 2004; Accepted: June 25, 2005

Correspondence: Pau-Choo Chung, Professor  
Department of Electrical Engineering, National Cheng  
Kung University, Tainan, Taiwan  
E-mail: pcchung@ee.ncku.edu.tw

becomes a barrier to the diagnosis accuracy especially for less-experienced physicians. Reports show that currently, the diagnosis can only achieve 85% accuracy and most radiologists encourage biopsies for the final diagnosis. To resolve these problems, it is especially very important to use the computer-aided system [2-3].

In recent years, a few researchers have used different approaches to do the detection and classification of masses. In 1989, Lai et al. used image enhancement and template-match to detect circumscribed masses [4], but the method mentioned is limited to circumscribed masses only. In 1990, Brzakovic et al. used thresholding and Fuzzy pyramid linking algorithm in doing the segmentation and detection of masses on the 256\*256 size ROI, and then further classifying masses as benign, malignant or nontumor [5] depending on the morphological feature of the segmented object. In their 25 samples used for evaluation the correct classification was achieved in 85% of the cases. Some researchers had also proposed the use of asymmetry of two sides of breast to determine the location of masses. As Yin et al. had done manually aiming at the left and right breast images, after that the information obtained in the reciprocal deduction of linear and non-linear of the left and right breast images were then used to detect the location of masses [6]. The texture features were also used as the key characteristics for differentiating between the masses and the normal tissues. Kagelmeyer et al. [7] used local edge characteristic and texture feature to detect speculated masses. Chen et al. [8] and Wei et al. [9] also used texture features and linear discrimination to classify between masses and normal texture. Christoyianni et al. [10] proposed a computer-aided system consisted of the image preprocessing, feature extraction, neural network classifier, and decision criteria for the identification of circumscribed mass.

Up to this moment masses detection from digitized mammograms is still very challenging. The main reason is caused by that the masses usually mix with the inhomogeneous tissues in the breast. The gray levels of those inhomogeneous tissues in the breast could vary with the distribution of breast soft tissue. Furthermore, the difficulty could be increased due to that the masses shown in digitized mammograms are similar to the glands, cysts or dense portions of the breast [11]. Hence, the intensity of the background may be higher than those of the masses in some cases causing the miss detection by using histogram statistic as the feature. Though generally the density and gray levels of the masses are higher than the surrounding tissues, some mass images have unclear lesion boundary and the contrast between the mass edges and the backgrounds is low. Moreover, some mass images might be covered by the background tissues. These

phenomenons increase the difficulty in the detection of masses. As shown in Fig. 1, the region within the circle has been proved as a mass, but still this cannot be visually observed from the image. In such a case, the masses may not be found by simply using the thresholding segmentation method proposed by some researchers in the past.

Comparing with using the variation of gray levels or the contrast of intensities, using the variation of texture features is reportedly more reliable in the detection of masses [12-13]. Based on this consideration, our system uses textures for the discrimination of edge, background and mass blocks from the ROIs. The texture features adopted are Second-order joint probability SGLD based on the co-occurrence matrix utilizing various distance and angle of the gray level pair, and the Fractal Dimension, due to their reportedly excellent performance on microcalcification detection [14].

For the mass classifications, the main cause of difficulty is arisen by the diversification of features. In clinical diagnosis, the signs of abnormality observed by expert radiologists are very diverse. They include the size, contrast, intensity, density and shape of edges. According to this reason, the integration ability of various features has to be considered for designing the Computer-aided System. In the past years, some researchers used templates to code the geometric structures of specific types of masses, then, matched those template patterns from a mammogram. With this approach, their methods are limited to only certain specific types of masses, such as circumscribed masses or spiculated masses. All these years, the neural network is regarded as one prominent tool for training a system as a classifier. The neural network uses simple connection of the artificial neurons to imitate the neurons in human. It also has a huge capacity of parallel computing and powerful remembrance ability. Based on the mentioned reasons, in this proposed system the obtained texture features are entered into the PNN as the input vectors, to train the PNN for the classification of blocks into edge, mass and background blocks. The area containing the mass blocks and the edge blocks is then considered as the mass suspicious area.

According to the medical literatures, shape feature is one of the most important features used for differentiating malignant from benign masses, and therefore it will also be adopted as one of the features for mass malignancy and benignancy classification. However, it should be noted that the accuracy of segmentation significantly affects the extraction of shape features. The results acquired from the PNN are far from enough accurate for shape calculation. Thus Entropic-thresholding methods were used in the mass segmentation module to obtain fine-segmented masses

from the suspicious area. With the fine segmentation being operated only on the suspicious area detected in the previous module, it also greatly reduces the noise effect caused from background. Finally, in the mass classification module, four kinds of shape features including circularity, contrast, radial angle and FWHM (Full Width at Half Maximum) were then applied to a neural network system for classifying the masses as benignancy or malignancy.

A diagram of this developed system is shown as Fig. 2. In Preprocessing Module, the ROI firstly undergoes a preprocessing to remove noise effects and enhance the useful information. Then, the spatial gray level difference matrix (SGLDM) and Fractal dimension are used as the features of the image. The obtained features are then entered into the PNN, so called Mass Detection Module to train the PNN for the mass detection. Then, the Mass Segmentation Module is applied for the segmentation of the mass by using Local Entropy method. Finally, in Mass classification Module, the mass regions that were successfully segmented were further classified as benign or malignant disease by using another PNN with inputs of the texture and the shape features of the segmented masses.



Fig 1. An example of mammogram

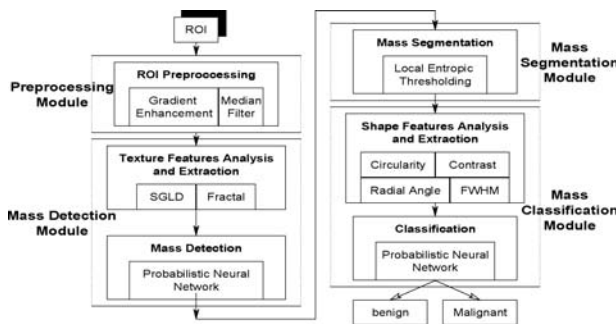


Fig 2. System diagram

## 2. ROI PREPROCESSING

One of major mammographic characteristics for mass detection is texture. Unlike detection of microcalcifications which can be detected effectively by mammograms, masses are part of breast issues and have characteristics very similar to their surroundings which present more challenges than microcalcification detection. In general, the pixels representing masses tissues have higher gray-level intensities compared to their surrounding background. In this section, a two-stage preprocess consisting of gradient enhancement and median filter-based smoothing is proposed. The first stage enhances gradient values of pixels with high intensities which are assumed to be potential mass pixels. Then, the second stage makes use of a median filter to eliminate the noise in the image background. Despite the fact that the size of a digitized mammogram is generally very large, normally about pixels, the regions of interest (ROIs) are usually very small and limited to areas being determined as suspicious regions of masses such as one shown in Fig. 3 compared to the original size of the mammogram in Fig. 4. Therefore, the first step of preprocessing is to segment the ROIs from the image background so that the image processing will not be overwhelmed and dominated by the large image background.

### 2.1 Gradient Enhancement

In order to separate suspicious masses from background, a gradient enhancement technique is used to increase the gradient values of mass pixels by the following procedure.

$$I_1(x, y) = \text{gradient enhancement}\{I(x, y)\} \\ = g(x, y) + I(x, y) \quad (1)$$

where  $I(x, y)$  is the gray level value of the pixel located at the spatial position  $(x, y)$  of an image  $I$  with the gray level range  $G = \{0, 1, \dots, L-1\}$  and  $g_1(x, y)$  is the gray level value of the gradient of the pixel  $(x, y)$  calculated using a  $3 \times 3$  mask window with  $(x, y)$  as the center pixel by

$$g(x, y) = \frac{1}{9} \sum_{i=-1}^1 \sum_{j=-1}^1 |I(x+i, y+j) - I(x, y)| \quad (2)$$

Since the mammographic appearance of mass generally has higher intensities than that of their neighboring pixels,  $I_1(x, y)$  resulting from Eq. (1) can enhance gray-level intensities of mass pixels. Fig. 5 shows an enhanced image  $I_1(x, y)$  of the ROI in Fig. 3 using Eq. (1) where the mass is slightly enhanced compared to that in original image  $I$  in Fig. 4.

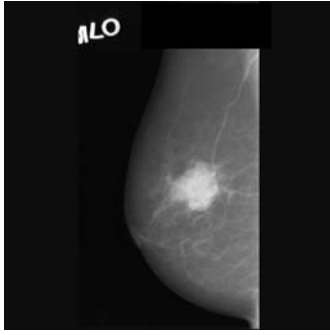


**Fig 3. Digital mammogram**

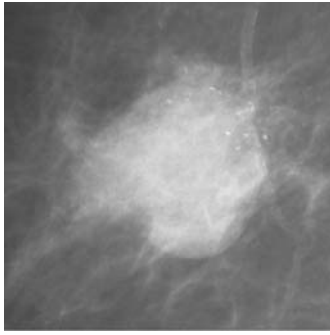


**Fig 4. Enlarged region of interest**

## 2.2 Removal of Noise Effects

In the previous stage the gradients of pixels with high intensities were enhanced. However, on some occasions, noise pixels will be also enhanced as well. In order to cope with this dilemma, a median filter is then used to remove these unwanted noise pixels by

$$I_2(x, y) = \text{median}\{I_1(x, y)\} \\ = \text{median}\left\{\sum_{i=-1}^1 \sum_{j=-1}^1 I_1(x+i, y+j)\right\} \quad (3)$$

where the medial filter is performed using a  $3 \times 3$  window Fig. 6 shows the result obtained by applying Eq. (3) to the enhanced image in Fig. 5. Since noise pixels generally have little correlation with mass pixels, the median filter used in the image  $I_2$  can smooth out these pixels so as to reduce their effects.

## 3. TEXTURE FEATURE EXTRACTION

After the ROI extraction, the next step is to segment masses from the background in accordance with texture features. This is because the textures of masses generally present distinct features from that of

normal breast tissues. Two methods are developed in this section for texture feature extraction, Spatial Gray Level Difference Matrix (SGLDM) [15-17] and fractal dimension [18]. In doing so the extracted ROI is divided into  $R \times R$  non-overlapping blocks where the size of the image block must be properly determined. If the block is too small, the difference of the mass textures from normal textures cannot be well characterized. If it is too large, the result may be too coarse. According to our experiments, the best size of the image block is found to be  $32 \times 32$  pixels. A diagram of the proposed texture feature extraction is depicted in Fig. 7 where an image is divided into  $R \times R$  non-overlapping blocks, each of which will be processed for texture feature extraction separately.

### 3.1 SGLDM

The SGLDM has been widely used for texture analysis. It is based on the spatial gray-level co-occurrence matrix of an image  $I$ , which is an  $L \times L$  dimensional matrix  $W=[t_{ij}]_{L \times L, d, \theta}$  with elements  $t_{ij}$  defined by

$$t_{ij} = \sum_{l=1}^M \sum_{k=1}^N \delta(l, k) \quad (4)$$

where  $\delta(l, k) = 1$ , if  $I(l, k) = i$ ,  $I(l + d \cos \theta, k + d \sin \theta) = j$ ;  $\delta(l, k) = 0$ , otherwise. It should be noted that  $t_{ij}$  represents a total number of transitions from gray level  $i$  to gray level  $j$ ,  $d$  represents the distance and  $\theta$  is the angle of the gray level pair. In this paper,  $d$  is chosen to be 4, and  $\theta$  to be  $45^\circ$  and  $135^\circ$ . In this case, the gray level pair of pixel at  $(x, y)$  in the co-occurrence matrix is  $(x+4, y+4)$  and  $(x+4, y-4)$ . Normalizing Eq. (4) by the total number of gray-level transitions,

$\sum_{i=0}^{L-1} \sum_{j=0}^{L-1} t_{ij}$ , we obtain a second-order joint probability for any gray level pair  $(i, j)$ ,  $S_{d, \theta}(i, j)$  as

$$S_{d, \theta}(i, j) = \frac{t_{ij}}{\sum_{i=0}^{L-1} \sum_{j=0}^{L-1} t_{ij}} \quad (5)$$

By virtue of Eq. (5) four feature descriptors can be derived and defined as follows

$$\text{Energy}(S_{d, \theta}(i, j)) = \sum_{i=0}^{L-1} \sum_{j=0}^{L-1} [S_{d, \theta}(i, j)]^2 \quad (6)$$

$$\text{Inertia}(S_{d, \theta}(i, j)) = \sum_{i=0}^{L-1} \sum_{j=0}^{L-1} [S_{d, \theta}(i, j)(i - j)^2] \quad (7)$$

$$\text{Intensity}(S_{d, \theta}(i, j)) = \sum_{i=0}^{L-1} \sum_{j=0}^{L-1} [ij S_{d, \theta}(i, j)] \quad (8)$$

and



$$\text{Entropy}(S_{d,\theta}(i,j)) = -\sum_{i=0}^{L-1} \sum_{j=0}^{L-1} S_{d,\theta}(i,j) \log S_{d,\theta}(i,j) \quad (9)$$

In order to illustrate the performance of these four texture feature descriptors, 45 biopsy-proven mammogram cases were selected from the Taichung Veterans General Hospital and used for experiments. Each of these 45 cases contains three images representing background, edge and mass respectively.

### 3.1.1 Energy

The energy descriptor described by Eq. (6) captures the variance of gray-level variations between pixels along the direction and displacement  $d$ . If the gray-level distribution is wide spread, the  $S_{d,\theta}(i,j)$  will be small and so is  $\text{Energy}(S_{d,\theta}(i,j))$ . Fig. 8 shows the  $\text{Energy}(S_{d,\theta}(i,j))$  distributions for background, edge and mass for each of the 45 mammogram cases. As we can see from the figure, the  $\text{Energy}(S_{d,\theta}(i,j))$  distribution of background is lower than that of mass, but higher than that of edge. In order to improve better discrimination, a normalization procedure can be performed by clipping those values greater than 0.035 to 1, while the values below 0.035 are transferred by the linear transfer function  $s = T(r)$  as shown in figure

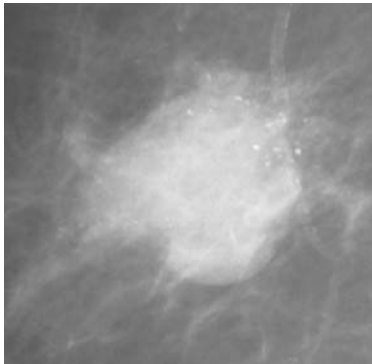


Fig 5. Enhanced ROI

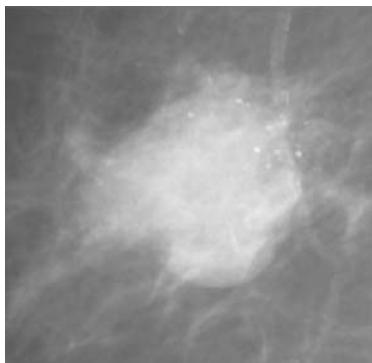


Fig 6. Noise removed ROI

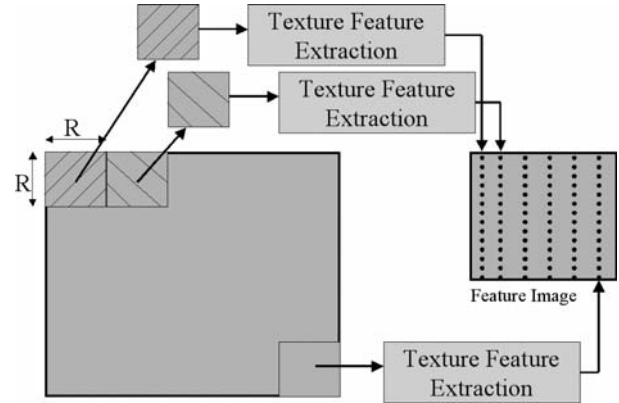


Fig 7. Feature extraction

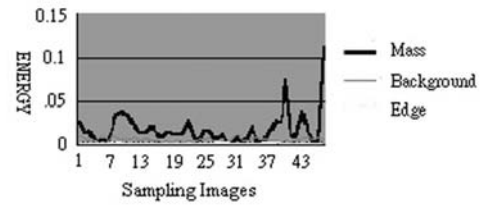


Fig 8. Energy distribution of masses, backgrounds and edges.

9(a), where  $s$  and  $r$  represents the energies after and before transformation respectively. Fig. 9(b) shows the normalized energy distributions where the three energy distributions are now better separated.

### 3.1.2 Inertia

The Inertia descriptor provides another means of capturing features of gray-level variations. When an image such as background is smooth, the change in gray levels is small. As a result, the values of the co-occurrence matrix will be clouded along the diagonal line, which result in smaller inertia values. On the other hand, an image such as edge has sudden changes in gray level, the values of the co-occurrence matrix will be wide spread from the diagonal line. In this case, the resulting inertia values will be large. The same 45 mammogram cases were used for our experiment. Since the range of the inertia values for edge was very high, a normalization procedure that was used in the energy distribution was necessary. The normalization is performed such that the values greater than 700 are set to 1 and values smaller than 100 to 0. Fig. 10 shows the normalized inertias for edge, background and mass, illustrating that the inertia distribution of edge was generally higher than that of background and mass. Furthermore, it has higher variation from case to case since different edge images had very much different

inertia values. Fig. 10 also shows that except a few cases, the inertia distribution of mass has higher values than that of background.

### 3.1.3 Intensity

Intensity descriptor measures the brightness of an image. Generally, masses are brighter than backgrounds in mammograms. As a result, the changes in gray-level of mass will occur in the lower right quadrant of the co-occurrence matrix. Therefore, the intensity distribution of mass will be higher than that of edge and background. Fig. 11 shows that the values of the 45 mammogram cases produced by the Intensity descriptor for mass, edge and background after the intensity values were normalized as we did for the Energy and Inertia descriptors. As expected, the intensity distribution of mass had highest values among these images.

### 3.1.4 Entropy

The concept of entropy is derived from information theory, which can be used to measure the information (i.e., uncertainty) contained in a source. A larger value of entropy value indicates the source is more unpredictable, thus its probability distribution is more likely widely distributed. By taking advantage of entropy the Entropy descriptor can describe how much uncertainty produced by each of edge, background and mass. Since background pixels are generally more uniformly distributed compared to mass pixels that appear in more confined areas, the values of the entropy distribution of background should be higher than that of mass. On the other hand, the unpredicted nature of edge pixels usually results in very high values of entropy distribution. These phenomena are illustrated in Fig. 12, which shows the normalized entropy distributions of the 45 mammogram cases for edge, background and mass.

## 3.2 Fractal Dimension

For fractal computation, a 2D image  $I(x,y)$  is reconstructed into a 3D curved surface  $(x,y,I(x,y))$  where  $(x,y)$  is the coordinate of image, and  $I(x,y)$  is the gray level at  $(x,y)$ . Using the 3D curved surface to calculate the volume, called surface area between an upper blanket and a lower blanket from which the fractal dimension (FD) can be derived. The surface area can be estimated by measuring the volume between an upper blanket,  $U_r(x,y)$  defined by

$$U_r(x,y) = \max\{U_{r-1}(x,y) + 1, \max_{|(i,j)-(x,y)| \leq r} U_{r-1}(x,y)\} \quad (10)$$

and a lower blanket,  $L_r(x,y)$  defined by

$$L_r(x,y) = \min\{L_{r-1}(x,y) + 1, \min_{|(i,j)-(x,y)| \leq r} L_{r-1}(x,y)\} \quad (11)$$

where the initial  $U_0(x,y) = L_0(x,y) = I_0(x,y)$  and  $r$  is a distance above or below the surface which is also a scaling factor of FD. The surface area  $V(r)$  is then defined as the half of the volume increment by

$$V(r) = \frac{1}{2} \sum_{(x,y)} \{[U_r(x,y) - U_{r-1}(x,y)] + [L_r(x,y) - L_{r-1}(x,y)]\}. \quad (12)$$

Since  $V(r)$  is proportional to  $r$ , it can be represented as

$$V(r) = kr^{2-D} \quad (13)$$

with the  $D$  defined as fractal dimension (FD) which can be calculated based on  $\log V(r)$  versus  $\log r$  as follows.

$$D = 2 - \frac{\log V(r) - \log k}{\log r} \quad (14)$$

The volume  $V(r)$  can be viewed as an image surface with the variable specified by the scaling factor  $r$ , while  $D$  can be used as a measure of image texture characterization. However, it should be noted from Eq. (14) that the  $D$  is not directly related to  $r$  because the texture characteristics are weakly associated with  $r$ . Since an edge indicates sudden changes in gray level, its FD value should be small. On the other hand, the background is generally homogenous and its FD value

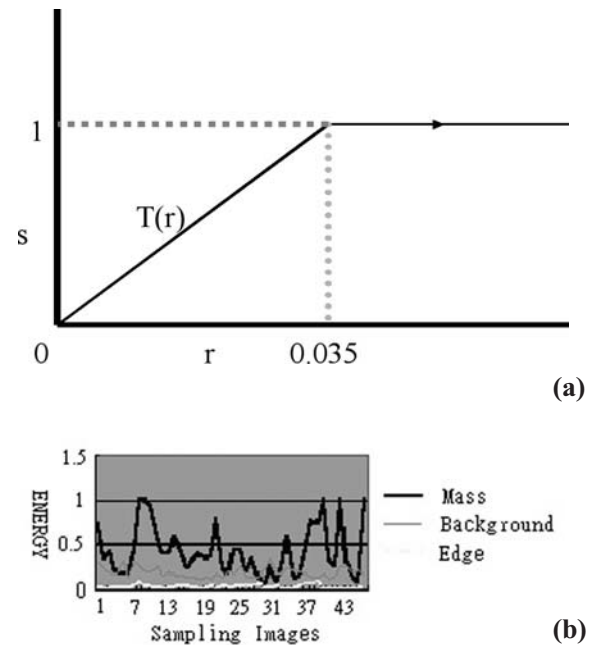


**Fig 9. (a) The transfer function of energy normalization. (b) Normalized energy distribution of masses, backgrounds and edges.**

should be large. Fig. 13 is the normalized FD distributions of the 45 mammogram cases used in the previous section where the FD distributions of the edge, background and mass were well separated.

## 4. MASS DETECTION AND SEGMENTATION

### 4.1 Mass Detection

In this section, the five obtained features acquired from block images are applied to the Probabilistic Neural Network (PNN), pixel by pixel, to train the PNN for masses detection. Also please be noted that the block used is  $32 \times 32$  pixels, so the feature image obtained from the  $512 \times 512$  pixels ROI is  $16 \times 16$  pixels.

The diagram of the PNN architecture is shown in Fig. 14 where there are 5 processing units in the input layer, 209 processing units in the hidden layer and 3 processing units in the output layer. The PNN takes as

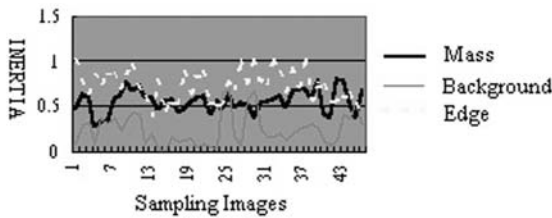


Fig 10. Normalized inertia distribution of masses, backgrounds and edges.

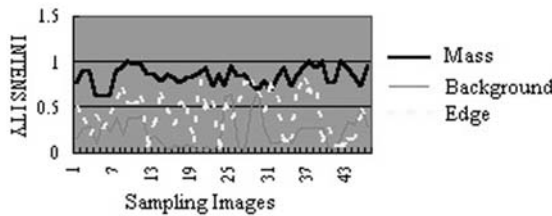


Fig 11. Normalized intensity distribution of masses, backgrounds and edges.

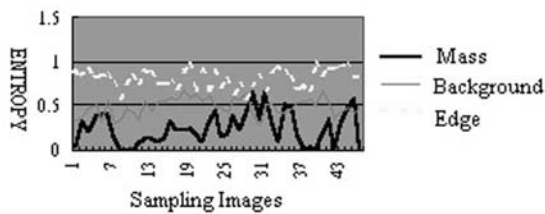


Fig 12. Normalized entropy distribution of masses, backgrounds and edges.

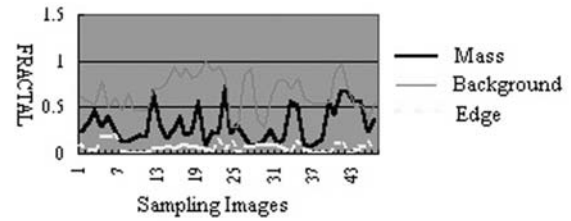


Fig 13. Normalized inertia distribution of masses, backgrounds and edges.

its inputs five texture features obtained from the five feature descriptors, Energy, Inertia, Intensity, Entropy, FD described in Section 3. Therefore, its input is a 5-dimensional texture feature vector ( $X_1, X_2, X_3, X_4, X_5$ ) generated from each of  $32 \times 32$  image blocks. The output layer of the PNN has three processing units which are used to classify three different types of images, edge, background and mass. If an output-processing unit has the highest value, the input block is regarded as its corresponding type. Fig. 15 is one of the output acquired from this PNN system by using Fig. 6 as the input. In Fig. 15, the white region indicates the mass, the gray region indicates the edge and the black region indicates the background texture. Due to the fact that image block is set as  $32 \times 32$  pixels, the obtained region from the PNN system is too coarse. The next section will present an improvement processing on the output result to get the finer segmentation of masses.

### 4.2 Mass Segmentation

According to the result in Section 4.1, the blocks in ROI can be detected and classified as masses, edges or backgrounds. The detected masses and edges shown from the outputs of the PNN system are the potential area of masses, which is called suspicious area. For this stage, the fine segmentation of masses within the suspicious areas is carried out using the Entropic Thresholding (ET) method. Assume that the gray level range is  $G = \{0, 1, \dots, L-1\}$ . Also let  $t$  be the threshold partitioning the gray levels  $G$  into the two regions  $G_0 = \{0, 1, 2, \dots, t\}$  and  $G_1 = \{t+1, \dots, L-1\}$ . The co-occurrence matrix  $W$  thresholded by  $t$  can be divided into four quadrants which represent background to background (BB), background to foreground (BF), foreground to background (FB) and foreground to foreground (FF) respectively provided that pixels with gray levels above  $t$  are assumed to be foreground pixels and otherwise are background pixels. Referring to reference [19], Assume that the probability of the four quadrants are  $p_{BB}(i, j)$ ,  $p_{BF}(i, j)$ ,  $p_{FB}(i, j)$  and  $p_{FF}(i, j)$ . Then, the entropies associated with the four quadrants can be defined as follows:



$$H_{BB}(t) = -\sum_{i=0}^t \sum_{j=0}^t p_{BB}(i, j) \log p_{BB}(i, j) \quad (15)$$

$$H_{BF}(t) = -\sum_{i=0}^t \sum_{j=t+1}^{L-1} p_{BF}(i, j) \log p_{BF}(i, j) \quad (16)$$

$$H_{FB}(t) = -\sum_{i=t+1}^{L-1} \sum_{j=0}^t p_{FB}(i, j) \log p_{FB}(i, j) \quad (17)$$

$$H_{FF}(t) = -\sum_{i=t+1}^{L-1} \sum_{j=t+1}^{L-1} p_{FF}(i, j) \log p_{FF}(i, j) \quad (18)$$

Since BB and FF depict the gray level translations between background to background and between foreground to foreground respectively, they represent local properties. Using Eqs. (15) and (18), a local entropy (LE) was defined by

$$H_{LE}(t) = H_{BB}(t) + H_{FF}(t) \quad (19)$$

Similarly, BF and FB represent the joint properties between background and foreground, a joint entropy (JE) can be also defined in the same fashion by

$$H_{JE}(t) = H_{BF}(t) + H_{FB}(t) \quad (20)$$

Therefore, an optimal local threshold is the one, indicated by  $t_{LE}$  which maximizes the local entropy given by Eq. (19), whereas, an optimal joint threshold is the one, indicated by JE threshold  $t_{JE}$  maximizing the JE by Eq. (20). More precisely,  $t_{LE}$  and  $t_{JE}$  can be represented by

$$t_{LE} = \arg\{\max_t H_{LE}(t)\} \quad (21)$$

and

$$t_{JE} = \arg\{\max_t H_{JE}(t)\} \quad (22)$$

From the result in reference [20], it is known that the threshold obtained from the Local Entropy in Eq. (21) is better than the Joint Entropy. Therefore, the Local Entropy was chosen in this paper. Fig. 16 is the result of applying the LE thresholding to Fig. 15.

## 5. DIAGNOSIS CRITERIA AND SHAPE FEATURE ANALYSIS

After mass detection it is important to classify whether it is malignant or benign. Several primary features such as shape, size, appearance, edges, volume and location of masses reported in Refs. [21-24] can be used as criteria for this purpose and described as follows.

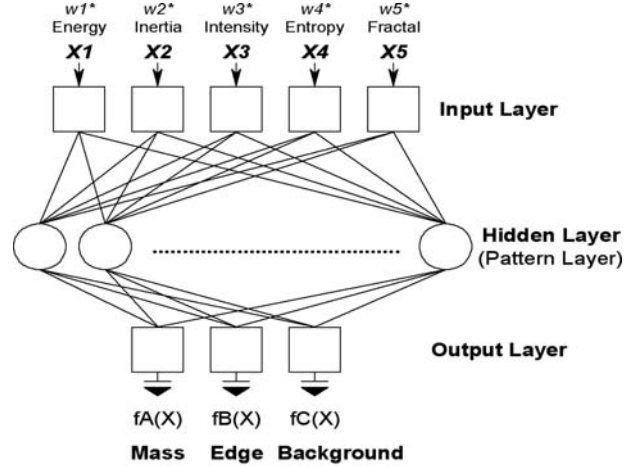


Fig 14. Texture feature recognizing in PNN

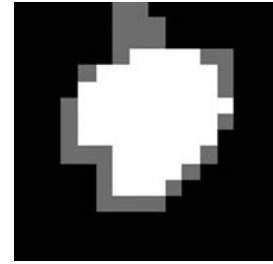


Fig 15. The output of PNN

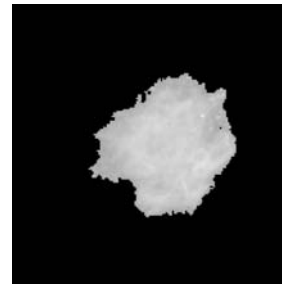


Fig 16. The result of Fig. 14 in LE thresholding segmentation

### 5.1 Malignant and Benign Criteria

#### 5.1.1 Malignancy Criteria

1. Spiculated masses are generally considered as a most obvious basis of diagnosis for early malignancy tumor.
2. The density of a malignant mass is generally high.
3. If one side of the edge of a mass is obscure and the other side is very clear, it could be malignant.
4. If the mammograms of right and left breasts

show asymmetrical density, it could be malignant.

5. If masses have nodes (specially tiny nodes, microlobular appearance) on the edge, it could fairly imply malignancy.

6. If microcalcifications are noted within the mass, malignancy should be highly suspected.

### 5.1.2 Benignancy Criteria

1. Mostly seen benign breast masses are fibroadenoma. The fibroadenoma and benign macrocyst are often clearly manifested benignancy in the mammogram, commonly shown as: having round and smooth edge, homogenous density in the mass, the surrounding breast texture is not affected and the breast structure usually will not be deformed (except the masses is very big).

2. If an image shows well-circumscribed masses (multiple lesions), usually it is benign fibroadenoma.

## 5.2 Shape Feature Extraction

As the criteria have implied, the texture feature and shape feature are two kinds of major features for the discrimination between the benign and malignant masses. In this section, four shape feature descriptors will be introduced, including circularity, contrast, radial angle and FWHM (Full Width at Half Maximum). These descriptors will be applied on the segmented mass for the shape feature extraction.

### 5.2.1 Circularity

The main purpose of circularity is to show the circular degree of masses [25]. The higher the circularity is, the more circular the object tends to be. Due to that the roundness is one of the criteria of benign masses, the probability of masses as being benign is higher when circularity is higher. Let  $R$  be defined as the region of masses and  $R'$  be the region of ROI outside the mass. In our computation of mass circularity, a circle  $C_{Eq}$  which has the same area as the mass is first located with its center being the center of the mass, as shown in Fig. 17. Then, the overlapping ratio of the circle and the mass is calculated as the circularity. The equations for calculating the Circularity are shown from Eq. (23) to Eq. (27) as

$$S = \sum_{(x,y) \in R} 1 \quad (23)$$

where  $S$  is the area of the mass, and the center of the mass,  $(\bar{x}, \bar{y})$ , is defined by

$$\bar{x} = \frac{1}{S} \sum_{(x,y) \in R} x \quad (24)$$

The radius of circle  $C_{Eq}$ ,  $R_{Eq}$  is represented as

$$\bar{y} = \frac{1}{S} \sum_{(x,y) \in R} y \quad (25)$$

$$R_{Eq} = \sqrt{\frac{area(C_{Eq})}{\pi}} = \sqrt{\frac{area(R)}{\pi}} = \sqrt{\frac{S}{\pi}} \quad (26)$$

Then finally the circularity can be calculated as follows.

$$circularity = \frac{area(R \cap C_{Eq})}{area(R)} \quad (27)$$

Please be noted that the circularity value would be between 0 and 1. If the ratio is 1, this means that the mass matches exactly with the  $C_{Eq}$ , implying the mass is circular. On the other hand, if the circularity is much smaller than 1, this implies the mass is far from a circle.

### 5.2.2 Contrast

Generally speaking, the intensities of malignant masses are higher than those of benign masses. Therefore, the contrast of masses with respect to the background in malignancy is higher than in benignancy. In our approach, the contrast is computed as the difference between the gray level average of masses and that of the tissue within a defined ring-like operator. As shown in Fig. 18, the ring-like operator indicates the circle band around the region of masses and can be represented as

$$\Omega = \{(x, y) | d \leq \sqrt{x^2 + y^2} \leq d + \Delta d\} \quad (28)$$

Here  $d$  is the radius of the smallest circle containing the mass,  $\Delta d$  is the width of the ring-like operator. According to the experiment result,  $\Delta d$  is set as 5. The Contrast is then computed as follows

$$contrast = \frac{\text{mean}\{R\} - \text{mean}\{\Omega\}}{\text{mean}\{R\}} \quad (29)$$

where  $R$  is the region of masses.

### 5.2.3 Radial Angle

The spiculation are usually an important indicator of the malignant masses. In this paper, the Radial Angle is used to differentiate the shape of edges of the masses as spiculated or as round and smooth. The Radial Angle is the smaller included angle  $\theta$  between the direction of the gradient and the radial direction of the edge, as revealed in Fig. 19, where the Radial Angle of P1 is  $\theta$ . As we know, when the mass tends to be more round, its Radial Angles tend to be near  $180^\circ$  and the average of the Radial Angles tends to be larger. Conversely, a mass with spiculated edge will have a smaller averaged Radial Angle.

Fig. 20 shows the histograms of the Radial Angles of a circle and of a region with speculated edge. From

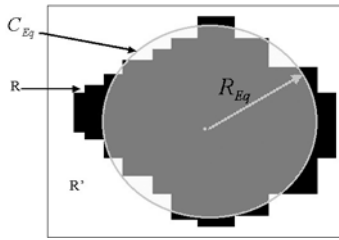


Fig 17. An example of circularity

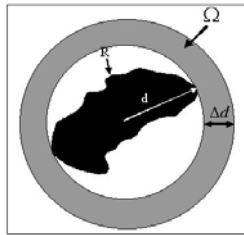


Fig 18. An example of contrast

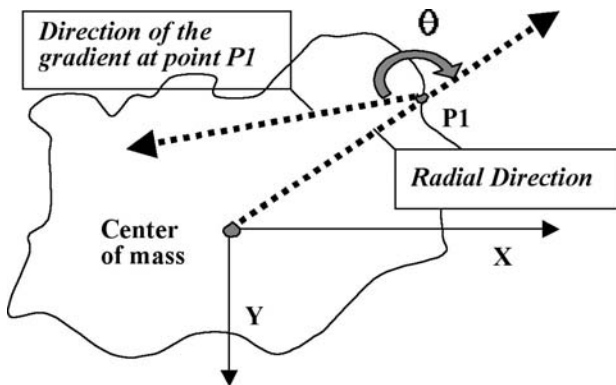


Fig 19. An example of Radial Angle

this figure, the distribution of the circular shape is aggregated around the largest value,  $180^\circ$ , while that of a spiculated shape is evenly distributed into the much smaller values. Therefore, the value of the averaged Radial Angles provides one indicator to the differentiation between benign and malignant masses.

#### 5.2.4 FWHM (Full Width at Half Maximum)

The Full Width at Half Maximum (FWHM), another feature widely used on optical engineering [26] computed from the histogram of the Radial Angles distribution can be used to differentiate the shape of edge of masses as regular or irregular. The FWHM is computed as the total number of angle values which have the histogram higher than half of the highest histogram value. When the histogram distribution is concentrated, the total number of angle values having

their histogram larger than half of the highest histogram is smaller. Conversely, when the histogram distribution is spread, this total number of angle values is larger. Since the more irregular a mass is, the wider its histogram distribution of the Radial Angles, consequently, we will have the larger FWHM value. Fig. 21 shows four examples of the histogram of the Radial Angles, where (a) and (b) are the spread Radial Angle histogram distributions, and (c) and (d) are concentrated Radial Angle distributions. From these figures, we can see that the FWHM would be larger for the cases in (a) and (b), and smaller for the cases in (c) and (d).

## 6. EXPERIMENTAL RESULT

The mammograms provided by the Taichung Veteran General Hospital, Taiwan, R.O.C., obtained from 84 different patients were used for experiment. A Fuji FD-R641 scanner was used to digitize these films with the resolution being 0.1mm between each pixel and 8 bits gray level per pixel. All the patterns have been proven by biopsy and 127 ROIs including 74 malignant ROIs and 53 benign ROIs were selected.

To evaluate the performance of the Mass Detection Module, each ROI is first divided into blocks, each of  $32 \times 32$  pixel size. Let  $N_p$  be the total number of positive blocks and  $N_n$  be the total number of negative blocks. Then we define TPN to be the number of blocks which contains masses and are actually detected, and FPN to be the number of blocks which contains no masses but were falsely detected. Then, the true negative number (TNN) and false negative number (FNN) can be defined by  $TNN = N_n - FPN$  and  $FNN = N_p - TPN$  respectively. Then, we can further define sensitivity (SS), specificity (SP) and positive predictive value (PPV) by  $SS = TPN/N_p$ ,  $SP = TNN/N_n$  and  $PPV = TPN/(TPN + FPN)$ . In our experimental evaluation, 10 benign ROIs and 14 malignant ROIs were selected according to their visibility of edges. The mass contours within these selected ROIs are delineated by radiologists and will be used later as the ground truth of mass detection. Each block inside the contour of mass is considered as a positive block and outside the contour of mass is considered as a negative block, while those blocks on the boundary are excluded. Then TPN could be counted as those white or gray blocks inside the contour of mass. TNN could be counted as those black blocks outside the contour of mass. FPN could be counted as white or gray blocks outside the contour of mass and FNN could be counted as black blocks inside the contour of mass.

The detection results produced by the Mass Detection Module are tabulated in Table I. From Table

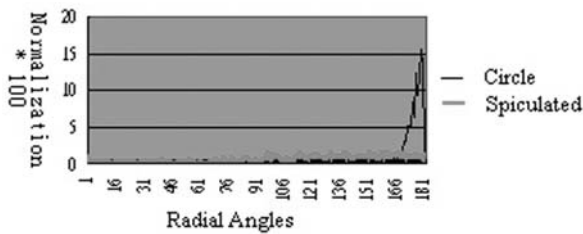


**Fig 20. Radial angle distribution of circle and speculated edges.**

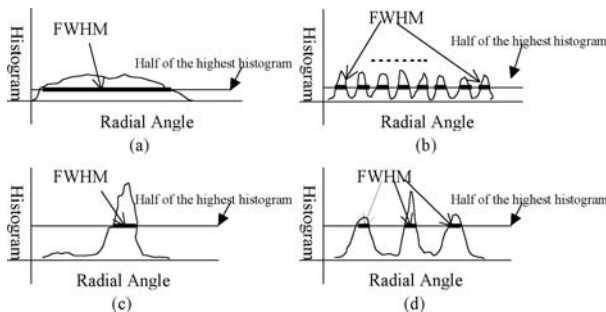


**Fig 21. Four examples of the radial angles histogram distributions**

I, we can see that the proposed approach presents promising results in detecting both benign and malignant masses with the SS, SP and PPV being 0.906, 0.862 and 0.867, respectively, for benign ROIs, and 0.895, 0.958 and 0.940, respectively, for malignant ROIs. However, we can still observe that the proposed approach has a slight better performance in detecting malignant masses than benign masses.

In order to evaluate the proposed system, the receiver operating characteristic (ROC) analysis was also used for performance evaluation and area under the ROC curve, Az, is used as the measure indicator. The larger the Az is, the higher performance the system shows.

Table II shows the Az value when each single texture feature and shape feature is used in the third column. The fourth column shows the average Az values of texture features and the shape features, while the fifth column is the average Az value for all features. From Table II, we can see that the Radial Angle shows the best performance with 0.7523 of Az value. Furthermore, the shape feature has higher averaged Az value 0.6818 than the texture feature 0.6128. The total average Az value is 0.6432.

For the result of final experiment, the proposed system takes all features mentioned above as the input vector to the PNN which based on the training data to estimate the probabilistic density function of each

classification. Fig. 22 shows the diagram of this PNN masses classification module, where input vectors  $X_i$  to  $X_9$  were the 4 shape features and 5 texture features. 45 ROIs were selected as training patterns from data set, including 24 malignant masses and 21 benign masses. The remaining 82 ROIs, including 50 malignant masses and 32 benign masses, are used as the testing patterns. The ROC curve of TPF versus FPF is plotted in Fig. 23 where the Az is equal to 0.93. Manifestly, integrating all the features into a PNN for classification illustrates much higher efficiency than any single feature in Table II.

Using TPN, FPN, TNN and FNN defined above, the detection rate (DR) defined by  $DR = TPN/\text{number of malignant cases}$ , false alarm rate (FAR) defined by  $FAR = FPN/\text{number of benign cases}$ , and correct classification rate (CR) defined by  $CR = (TPN+TNN)/\text{total number of cases}$ , can be computed. These results are also tabulated in Table III which has  $TPN=43$ ,  $FPN=6$ ,  $TNN=26$  and  $FNN=7$ , resulting in

$$DR = \frac{43}{50} = 86\%, \quad FAR = \frac{6}{32} = 18.75\% \quad \text{and} \quad CR = \frac{43+26}{82} = 84.15\%.$$

## 6. CONCLUSION

In this paper, a modular computer-aided system for detection, segmentation and classification of masses is presented. It is implemented by a two-stage preprocessing combined with a Probabilistic Neural Network to detect masses and the Entropic Thresholding for masses fine-segmentation. The preprocessing is particularly designed to enhance the gray-level intensity of suspicious masses and eliminate noise effects by making use of a median filter. In order to detect masses, five texture features are introduced for training the PNN to achieve the coarse mass detection. Based on the detected masses by the PNN, the Local Entropy thresholding is designed to extract masses from the ROI for obtaining the refined shape of masses. Due to that the shape of masses is the important characteristic for discriminating the mass as benign and malignant, the shape features are extracted from the fine-segmented masses for the classification of benign and malignant. Finally, the PNN was used again to classify masses as benign or malignant. From the experimental results, it shows that after the integration by PNN, the efficiency of classification of masses is better than any single feature.

The proposed system was designed as four individual modules, called Mammogram Preprocessing Module, Masses Detection Module, Masses



**Table I. Detection results of the mass detection module using 10 benign ROIs and 14 malignant ROIs respectively.**

	$N_P$	$N_n$	TPF	FPF	TNF	FNF	SS	SP	PPV
10 benign ROIs	1042	1047	944	145	902	98	0.906	0.862	0.867
14 malignant ROIs	807	2185	722	146	2039	85	0.895	0.958	0.940

**Table II. Az values of using single feature for masses classification**

Feature type	Feature	Az	Averaged Az	
Texture Feature	Energy	0.5668	0.6128	0.6432
	Inertia	0.5606		
	Entropy	0.5824		
	Intensity	0.6195		
	Fractal Dimension	0.7348		
Shape Feature	Contrast	0.7167	0.6813	
	FWHM	0.5791		
	Radial Angle	0.7523		
	Circularity	0.6771		

**Table III. Classification result**

TPN	FPN	TNN	FNN	DR	FAR	CR
43	6	26	7	86%	18.75%	84.15%

\* Total cases: 82, benign cases: 32, malignant cases: 50

Segmentation Module and Masses Classification Module where each module performs a specific task and can be easily upgraded and improved individually in the future. In order to evaluate this proposed system, a data set was used for test. The data set consists of 200 biopsy-proven ROI's provided by Taichung Veteran General Hospital, Taiwan, R.O.C. The results show that the system performs reasonably well at satisfactory level and has great promise in future clinical applications.

## ACKNOWLEDGEMENT

The authors would like to thank National Science Council and Taichung Veteran General Hospital, Taiwan, Republic of China for budget support under the Grant number NSC 88-2213-E-006-010 and TCVGH-915510D respectively.

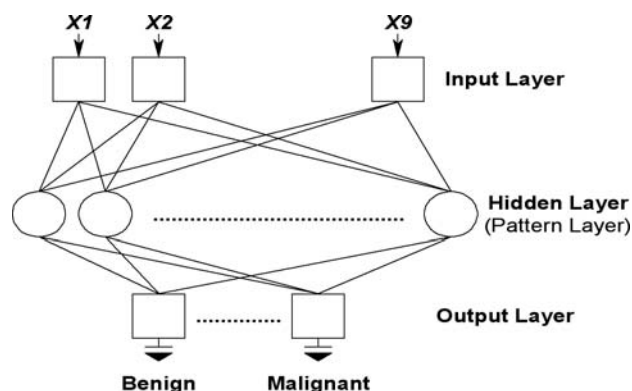


Fig. 22. Masses classification in PNN

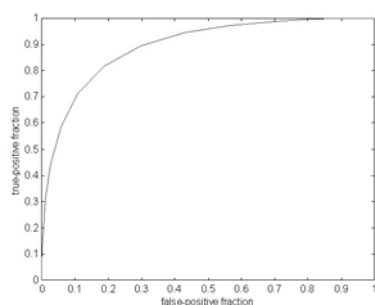


Fig. 23. ROC curve of the masses classification using 9 features as the input vector of PNN.

## REFERENCE

1. The National Breast and Cervical Cancer Early Detection Program, NBCCEDP, At-A-Glance, 1997 CDC U.S. Department of Health and Human Services.
2. Newsweek, pp. 64, May 10 1993.
3. C.J. Vyborny, "can computers help radiologists read mammograms," *Radiology* 1994; 191: 315-317.
4. S.M. Lai, X.B. Li and W. F. Bischof, "On techniques for detecting circumscribed masses in mammograms," *IEEE Trans. Med. Imag.* 1989; 8(4): 377-386.
5. D. Brzakovic, X.M. Luo and P. Brzakovic, "An approach to automated detection of tumors in mammograms," *IEEE Trans. Med. Imag.* 1990; 9(3): 233-241.
6. F.F. Yin, M.L. Giger, K. Doi, C.E. Metz, C.J. Vyborny and R.A. Schmidt, "Computerized detection of masses in digital mammograms: Analysis of bilateral subtraction images," *Medical Physics* 1991; 18(5): 955-963.
7. W.P. Kegelmeyer Jr., J.M. Prunedu, P.D. Bourland, A. Hillis, M.W. Riggs And M.L. Nipper, "Computer-aided mammographic screening for spiculated lesions," *Radiology* 1994; 191(2): 331-337.
8. H.P. Chan, D. Wei, M.A. Helvie, B. Sahiner, D.D. Adler, M.M. Goodsitt, and N. Petrick, "Computer-aided classification of mammographic masses and normal tissue: Linear discriminant analysis in texture feature space," *Physical Medical Biology* 1995; 40(5): 857-876.
9. D. Wei, H.P. Chan, M.A. Helvie, B. Sahiner, N. Petrick, D.D. Adler and M.M. Goodsitt, "Classification of mass and normal breast tissue on digital mammograms: Multiresolution texture analysis," *Med. Phys.* 1995; 22(9): 1501-1513.
10. I. Christoyianni, E. Dermatas and G. Kokkinakis, "Fast Detection of Masses in Computer-Aided Mammography," *Signal Processing Magazine, IEEE* 2000; 17(1): 54-64.
11. E. S. de Paredas, "Radiographic breast anatomy: Radiologic signs of breast cancer," *RSNA Categorical Course Phys.* 1994; 1: 35-46.
12. K. Bovis, S. Singh, "Detection of masses in mammograms using texture features," *Proceedings of 15th International Conference on Pattern Recognition* 2, 267-270, Sept. 3-7 2000.
13. M. Sameti, R.K. Ward, B. Palcic, J. Morgan-Parkes, "Texture feature extraction for tumor detection in mammographic images," *IEEE Pacific Rim Conference on Communications, Computers and Signal Processing* 2, 831-834, Aug. 20-22 1997.
14. C.S. LO, P.C. Chung, S.K. Lee, C.I. Chang, T. Lee, G.C. Hsu and C.W. Yang, "Off-Line Mammography Screening System Embedded with Hierarchically-Coarse-to-Fine Techniques for the Detection and Segmentation of Clustered Microcalcifications," *IEICE Trans. on Information and Systems* E83-D(12), 2161-2173 (2000).
15. B. Aldrich and M. Desai, "Application of Spatial Grey Level Dependence Methods to Digitized Mammograms," *Proceedings of the IEEE Southwest Symposium on Image Analysis and Interpretation*, 100-105, April 21-24 1994.
16. H.P. Chan, K. Doi, S. Galhotra, C.J. Vyborny, H. MacMahon and P.M. Jokich, "Image feature analysis and computer-aided diagnosis in digital radiology: Automated detection of microcalcifications in mammography," *Med. Phys.* 1987; 14(4): 538-548.
17. A.P. Dhawan, G. Buelloni and R. Gordon, "Enhancement of mammographic features by optimal adaptive neighborhood image processing," *IEEE Trans. on Med. Imag* 1986; MI-5(1): 8-12.

18. B.B. Mandelbrot, "The Fractal Geometry of Nature," Freeman, New York (1977).
19. P.S. Liao, B.C. Hsu, C.S. Lo, P.C. Chung, T.S. Chen, S.K. Lee, L. Cheng and C.I. Chang, "Automatic Detection of Microcalcifications in Digital Mammograms by Entropy Thresholding," Proceeding of 18th Annual International Conference IEEE Engineering in Medicine and Biology Society, 88-89, October 31-November 3 1996.
20. N.R. Pal and S.K. Pal, "Entropic thresholding," Signal processing 1989; 16: 97-108.
21. G. Cardenosa, "Breast Imaging Companion 2/ed," Williams & Wilkins (2001).
22. D.B. Kopans, "Breast Imaging 2/ed," Lippincott-Raven (1998).
23. D.B. Kopans, "Standardized mammography reporting," Radiologic Clinics of North America 1992; 30(1): 257-264.
24. C.J. D'Orsi and D. B. Kopans, "Mammographic feature analysis," Semin Roentgenol 1993; 28: 204-230.
25. N. Petrick, H.P. Chan, B. Sahiner and D. Wei, "An Adaptive Density-Weighted Contrast Enhancement Filter for Mammographic Breast Mass Detection," IEEE Trans. on Med. Imag 1996; 15(1): 59-67.
26. J. Kraus and P.P. Deimel, "Full-Width-Half-Maximum and Confinement of Optical Modes in Multiple-Quantum-Well Laser Structure," Journal of LightWave Technology , IEEE 1993; 11(11): 1802-1805.